Amyloid pathology impairs homeostatic inhibitory synaptic plasticity

Suraj Niraula[1], Shirley ShiDu Yan[1,2], Jaichandar Subramanian[1*]

[1]Department of Pharmacology and Toxicology, School of Pharmacy, University of Kansas, Lawrence, KS 66045, USA

[2]Department of Surgery, Vagelos College of Physicians and Surgeons of Columbia University, New York, NY 10032, USA

[*] Corresponding authors: jaichandar@ku.edu

Abstract

Alzheimer's disease is associated with altered neuronal activity, presumably due to impairments in homeostatic synaptic plasticity. Neuronal hyper and hypoactivity are also observed in mouse models of amyloid pathology. Using multicolor two-photon microscopy, we test how amyloid pathology alters the structural dynamics of excitatory and inhibitory synapses and their homeostatic adaptation to altered experience-evoked activity in vivo in a mouse model. The baseline dynamics of mature excitatory synapses and their adaptation to visual deprivation are not altered in amyloidosis. Likewise, the baseline dynamics of inhibitory synapses are not affected. In contrast, despite unaltered neuronal activity patterns, amyloid pathology leads to a selective disruption of homeostatic structural disinhibition on the dendritic shaft. We show that excitatory and inhibitory synapse loss is locally clustered under the nonpathological state, but amyloid pathology disrupts it, indicating impaired communication of changes in excitability to inhibitory synapses.

Introduction

The balance between excitation and inhibition (E/I) maintains neuronal activity levels within a narrow range. Homeostatic synaptic plasticity mechanisms compensate for alternations to neuronal excitability (Turrigiano, 2012). However, neuronal hyperactivity has been observed early in Alzheimer's disease (AD) patients and mouse models suggesting an impairment in maintaining neuronal activity homeostasis (Busche and Konnerth, 2016; Palop and Mucke, 2016; Frere and Slutsky, 2018). Furthermore, progressive reduction in excitatory synapses and neuronal activity indicates that loss of excitability associated with synapse loss may not be compensated for by homeostatic plasticity mechanisms. This failure may stem from multiple causes, such as impaired detection changes to excitability or disruption in responding to altered excitability through synaptic plasticity mechanisms (Styr and Slutsky, 2018).

Structural homeostatic synaptic plasticity *in vivo* is typically studied in sensory cortices by altering sensory experience-evoked activity (Gainey and Feldman, 2017; Lee and Kirkwood, 2019). Under nonpathological conditions, sensory deprivation leads to structural homeostatic plasticity of excitatory and inhibitory synapses, favoring increased excitability of adult cortical neurons *in vivo*. Visual deprivation increases the strength and size of excitatory synapses in the visual cortex and modulates their dynamics (Goel and Lee, 2007; Keck et al., 2008; Hofer et al., 2009; Coleman et al., 2010; Keck et al., 2013; Barnes et al., 2017; Zhou et al., 2017; Sammons et al., 2018; Sun et al., 2019). In addition, adult layer 2/3 neurons exhibit increased loss of inhibitory synapses following visual deprivation (Keck et al., 2011; Chen et al., 2012; van Versendaal et al., 2012; Villa et al., 2016; Niraula et al., 2023), and mature excitatory synapses become less dynamic (Subramanian et al., 2019).

In vivo multiphoton imaging of structural synaptic dynamics in mouse models of AD thus far is limited to dendritic spines and axonal boutons (Liebscher and Meyer-Luehmann, 2012; Dorostkar et al., 2015; Subramanian et al., 2020). These studies reveal increased synaptic dynamics favoring their loss, particularly closer to amyloid plaques though the phenotype varies depending on the age, mouse strain, or the brain regions examined (Subramanian et al., 2020). How amyloid disrupts inhibitory synapses is less understood and remains controversial (Jimenez-Balado and Eich, 2021; Melgosa-Ecenarro et al., 2023). Though amyloid accumulates in the boutons of inhibitory neurons, the basal structural dynamics of these boutons are not significantly altered (Ruiter et al., 2021). However, some studies but not others have found axonal degeneration of inhibitory neurons and structural synapse loss (Garcia-Marin et al., 2009; Palop et al., 2011; Mitew et al., 2013; Kiss et al., 2016; Schmid et al., 2016; Umeda et al., 2017; Hollnagel et al., 2019; Petrache et al., 2019; Ruiter et al., 2020; Shimojo et al., 2020; Sos et al., 2020; Montero-Crespo et al., 2021; Kurucu et al., 2022; Niraula et al., 2023; Scaduto et al., 2023). A challenge to studying inhibitory postsynaptic dynamics *in vivo* is that they are primarily present in the dendritic shaft of excitatory neurons and lack a morphological surrogate, such as dendritic spines, which are typically used as a proxy for excitatory synapses. However, most dynamic spines carry immature excitatory synapses; therefore, how amyloid influences mature excitatory synapse dynamics *in vivo* remains unclear. Consequently, whether amyloid pathology disrupts structural homeostatic plasticity of mature excitatory or inhibitory synapses *in vivo* is not known.

Using a synaptic labeling approach that reliably detects mature excitatory and inhibitory synapses of cortical neurons and *in vivo* multicolor two-photon imaging, we show that the baseline dynamics of mature excitatory and inhibitory synapses are not altered in the visual

cortex of a mouse model of AD (hAPP mice - J20 line (Harris et al., 2010)). Interestingly, visual deprivation-evoked homeostatic plasticity of inhibitory synapses is disrupted in these mice. In contrast, reduced excitatory synaptic dynamics associated with visual deprivation are preserved, indicating that neurons in amyloid pathology retain their ability to sense changes in excitability. We show that impaired inhibitory homeostatic adaptation is not due to altered neuronal activity patterns but could stem from the impaired local coupling of excitation and inhibition, manifested as a reduced spatial clustering of the loss of excitatory and inhibitory synapses.

Methods

Mice

The University of Kansas Institute of Animal Use and Care Committee has authorized all animal procedures and complies with the NIH standards for the use and care of vertebrate animals. Transgenic hAPP mice overexpressing a mutant human form of amyloid precursor protein (APP) that encodes hAPP695, hAPP751, and hAPP770 bearing mutations linked to familial AD [APPV717F (Indiana), KM670/671NL(Swedish)], J-20 line were obtained from Jackson Laboratory). J20 mice and WT females from the same background were bred to generate heterozygotes for the hAPP transgene. J20 males and C57BL/6J-Tg (Thy1-GCaMP6s) GP4.3Dkim/J (Strain: 024275, JAX; (Chen et al., 2013)) females were bred to generate J20-GCaMP6s mice. Five mice at most were kept in a cage, but following cranial window surgery, they were individually housed on a 12h light/12h dark cycle or 24 hours darkness for visual deprivation experiments. Both genders were used in the study.

DNA constructs

The Cre-dependent TdTomato (pFudioTdTomatoW), Teal-gephyrin (pFudioTealgephyrinW), and PSD95-venus (pFudioPSD95venusW) plasmids were a kind gift from Dr. Elly Nedivi. The

pSIN-W-PGK-Cre plasmid is used to express Cre recombinase (Subramanian et al., 2013). The Cre-dependent expression of fluorescently labeled synaptic markers PSD95 and gephyrin have been shown to accurately represent excitatory and inhibitory synapses, respectively (Villa et al., 2016).

In-utero electroporation (IUE)

Timed pregnancies were established between heterozygous J20 males and WT females with the same genetic background. Half of the litter was heterozygous for the APP transgene, while the other half was WT (control). Using a 32-gauge Hamilton Syringe (Hamilton company), plasmids diluted in 1 µl of Tris-EDTA (1:1:0.5:0.15 molar ratios of pFudioTdTomatoW, pFudioTealgephyrinW, pFudioPSD95venusW, and pSIN-W-PGK-Cre, respectively) were injected in the lateral ventricle of E15.5 to E16.5 embryos. A square wave electroporator (ECM830, Harvard Apparatus) was used to deliver five pulses of 36 V (50 ms duration at 1 Hz) to a pair of platinum electrodes (Protech International) targeted at the visual cortex.

Cranial window

A cranial window was placed in 4-6-month-old J20 and WT mice over the visual cortex in the right hemisphere. An incision was made above the midline of the skull. The pericranium was softly scraped, and soft tissues were reflected laterally by blunt dissection. A biopsy punch was used to score a 5-mm-diameter circle covering the visual cortex. Using a fine drill and a sterile 0.5mm diameter round burr (Fine Science Tools), the skull was thinned along the scored circle. Fine forceps were used to carefully remove the bone flap, leaving the dura intact. A sterile, 5-mm diameter circular glass coverslip (Harvard Apparatus) was placed over the opening. To secure the coverslips in place, firm pressure was applied while Vetbond was placed over the area where the coverslip and bone met. Over the exposed skull, Metabond (C&B Metabond) was

placed and a titanium head post was attached to the window about two weeks following the surgery.

Optical intrinsic signal imaging

~14 days after cranial window surgeries, optical intrinsic signal imaging was performed to map the location of the visual cortex. A custom-designed upright microscope with a 4X objective (Nikon) was used for imaging. Mice were lightly sedated using isoflurane and positioned 20 cm in front of a high refresh rate monitor showing a horizontal bar drifting at 10 Hz. Images were captured at 5Hz with an sCMOS camera (1024 x 1024 pixels; Photometrics). The cortex was illuminated (500–600 m below the dura) using 610 nm light delivered by a fiber-coupled LED controlled by T-Cube LED drivers (Thorlabs). A 470 nm light was used to image reference vasculature. Cortical intrinsic signals were computed by extracting the Fourier component of light reflectance changes to matched stimulus frequency from downsized images (256x256 pixels). The magnitude maps were thresholded at 30% of the peak response amplitude. The fractional change in reflectance represents response magnitude. The magnitude maps were superimposed over the 470nm reference image to map the visual cortex.

Widefield calcium imaging

Instead of using intrinsic signal imaging to map the location of the visual cortex in GCaMP6s expressing mice, widefield calcium imaging was employed. The mapping methodology was comparable to intrinsic signal imaging, except fluorescence was imaged as opposed to reflected light. GCaMP6 was excited by an LED (Lambda FLED, Sutter) filtered through a bandpass filter (470/40, 49002 Chroma), and the emission was filtered with a 525/50 bandpass filter.

Two-photon imaging

Synaptic structural imaging was performed on isoflurane anesthetized mice with sparsely labeled neurons in the mapped visual cortex using a Sutter MOM multiphoton microscope. The Ti: Sapphire laser (MaiTai HP: Newport SpectraPhysics; 915 nm) was directed toward the microscope using table optics. A polarizing beam splitter and a rotating half-wave plate were used to regulate laser power. A pair of galvanometric mirrors scan the laser beams to the back aperture of the objective (Nikon 16X 0.8 NA). The output power from the objective was set to 40-50 mW. The same objective was used to gather the emission signal, which was then routed through appropriate bandpass filters (488/50, 540/50, and 617/73 for Teal, YFP, and TdTomato fluorescence, respectively) and three GaASP PMTs. Image acquisition was controlled by ScanImage (Vidrio Technologies), and images were obtained at 0.16Hz. The imaging field covered 133x133x~150 μm (1024 x 1024 XY pixels, Z step - 1 μm). For GCaMP6 imaging, neurons within the mapped visual cortex (~100-150 μm below the dura) were imaged at 4.22 Hz in head-restrained awake mice restrained in a body tube. The excitation wavelength was set to 940 nm, and the power was adjusted (20-40mW) to avoid signal saturation. The imaging field was a single Z frame of 336 x 336 um (256 x 256 pixels) consisting of ~50-100 cells.

***In vivo* synaptic imaging analysis**

The signal collected in each PMT (channel) is a combination of signals from the three fluorophores (Teal, Venus, and TdTomato) due to their overlapping emission spectra. We used spectral linear unmixing to reassign the signal from each fluorophore to the appropriate channel. Each image consisted of three channels, cell fill (TdTomato), PSD95 (Venus), and Gephyrin (Teal) channels. First, gephyrin and PSD95 puncta were marked if they were present in two consecutive frames and consisted of at least 8-9 or 4-5 clustered pixels, respectively, in mean-

filtered, volume-corrected images. For volume correction (normalization of the signal relative to local dendritic volume), we normalized the fluorescence in the synaptic channels to that of the cell fill channel. A normalization factor was calculated as the ratio of the mean pixel value of a chosen dendrite in the cell fill channel to the synaptic channel. Each pixel value in the synaptic channel was then multiplied by the normalization factor, and the pixel value of the cell fill channel was subtracted on a pixel-to-pixel basis. A custom-written 4D point tracking system implemented in Fiji using a modified version of the ObjectJ plugin (Villa et al., 2016) was used to transfer labeled markers (indicating each synapse type or no synapse) to matched locations on images from subsequent imaging sessions. Synaptic markers were transferred back to the identical location on the unmixed image for quantification. A custom-written macro was used to place a 5x5 pixel box (synaptic ROI) at the center of synaptic puncta for PSD95 on the spines and shaft gephyrin. The box overlapped with part of both puncta for dually innervated spines containing both PSD95 and gephyrin puncta. 5x5 pixel boxes (background ROI) were also placed on dendritic shaft locations lacking visible puncta to calculate background fluorescence. The background ROI boxes, equaling the number of identified synapses, were placed along the entire length of the dendritic segment used for synapse identification. PSD95 puncta on spines were classified as excitatory synapses based on a clustering index (CI_{PSD95}), which is calculated as

$$CI_{PSD95} = (F_{PSD95}/F_{cellfill})/(F_{bg\_PSD95}/F_{bg\_cellfill})$$

where F_{PSD95} and $F_{cellfill}$ are the mean fluorescence of synaptic ROI from PSD95 and cell fill channel of an identified puncta, respectively, and F_{bg_PSD95} and $F_{bg\_cellfill}$ are mean + 3x standard deviation of fluorescence of ten nearest background ROIs to that puncta. Similarly, $CI_{gephyrin}$ is calculated as

$$CI_{gephyrin} = F_{gephyrin}/F_{bg\_gephyrin}$$

where $F_{gephyrin}$ and $F_{cellfill}$ are the mean fluorescence of synaptic ROI and background ROI of the gephyrin channel, respectively. PSD95 and gephyrin are considered excitatory and inhibitory synapses if their clustering index is greater than one.

The gain and loss of a specific type of synapse between sessions were determined by calculating the number of newly formed puncta or lost puncta of that synapse type and dividing it by the total number of puncta of that synapse type in the later or previous session, respectively. Additionally, the distance of a synaptic puncta from the soma was calculated by summation of the distance of the puncta to the center of the nearest dendritic shaft and the distance from that point to the soma. To identify the nearest synapse, the distances of all synapses to each other were first calculated, and the nearest synapse was determined using the 'knnsearch' function in MATLAB. The nearest neighbor of both excitatory and inhibitory dynamic synapses was calculated using a similar approach.

We tracked 2453 $PSD95^+$ spines in WT mice and 2156 in hAPP mice, 1111 gephyrin puncta in WT, and 1073 in hAPP mice, across three imaging sessions. These structures were identified in 54 dendrites spanning a length of 4133 µm in WT mice and 48 dendrites spanning 3719 µm in hAPP mice. The synaptic density from the first imaging session for some of the analyzed hAPP neurons has been published (Niraula et al., 2023).

Calcium imaging analysis

The data on spontaneous calcium imaging is an independent analysis from the same raw data used for other analyses previously published (Niraula et al., 2023). Suite2p was used to perform motion registration and ROI detection on the time-series images (Pachitariu et al., 2017). If the soma was discernible in the mean or maximum projection picture, ROIs generated by Suite2p

were selected as cells (cellular ROI). The neuropil-corrected fluorescence (Fcorr) is calculated as F - (0.5xFneu). dF/F0 is calculated as (Fcorr – F0)/F0, where F0 is defined as the mode of the Fcorr density distribution. For each neuron, the mean dF/F0 over every three-second period was calculated for 228 seconds (76 x 3 seconds) and averaged. The percentage of neurons in each indicated dF/F0 bin was calculated as the number of neurons in that bin divided by the total number of identified neurons for each mouse. To assess functional connectivity in cellular ROIs obtained from Suite2p, we deconvolved spikes and applied a threshold (>2 SD from the mean) before binarizing the data. We then determined functional connections between pairs of neurons by comparing their coactive frames to a distribution generated from 1000 random circular shifts of their activity. Neuron pairs with coactive frames exceeding the 95th percentile of this distribution were considered functionally connected. We used the resulting functional connectivity matrix to determine the node degree of each neuron, which represents the number of edges (or connections) connected to that node over the entire imaging period. We calculated node degrees using MATLAB's graph and degree functions.

Statistics

Statistics were performed using SPSS or GraphPad Prism. P-values and statistical procedures are provided in the figure legends. $P<0.05$ is considered as significant.

Results

Selective disruption of homeostatic structural plasticity of inhibitory synapses on the dendritic shaft in amyloid pathology

To study how amyloid pathology influences the dynamics of excitatory and inhibitory synapses *in vivo*, we used an in-utero electroporation based synaptic labeling strategy that sparsely labels layer 2/3 cortical neurons in the visual cortex (Chen et al., 2012; Villa et al., 2016; Subramanian

et al., 2019). Three fluorescent proteins, TdTomato (cell fill), PSD95-venus (excitatory synaptic marker), and Teal-Gephyrin (inhibitory synaptic marker), were expressed in a Cre recombinase dependent manner (Figure 1A). Previous studies have shown that this approach reliably represents excitatory and inhibitory synapses in the same neurons *in vivo* along with dendritic spines (Chen et al., 2012; Villa et al., 2016). We used multicolor two-photon microscopy to image individual neurons expressing all fluorescent markers in the visual cortex *in vivo* under normal and visual deprivation conditions. Visual deprivation allows us to examine homeostatic structural synaptic plasticity associated with the reduced experience-evoked activity. To assess synaptic dynamics under baseline and altered experience conditions, we imaged the same neurons and synapses thrice with an interval of seven days between imaging sessions (Figure 1A,B). Between the first two imaging sessions, the mice were housed in a 12-hour light/12-hour dark cycle (baseline). Immediately following the second imaging session, mice were transferred to 24-hour darkness until the final imaging session (visual deprivation). The appearance of new synapses (gain) and disappearance of pre-existing synapses (loss) between the first two imaging sessions represents baseline dynamics, and between the second and third sessions includes changes associated with altered excitability (Figure 1C-G).

The synaptic labeling scheme allows us to detect four types of synaptic structures – dendritic spines with ($PSD95^+$ spines) or without ($PSD95^-$ spines) PSD95, gephyrin on dendritic shaft (inhibitory shaft synapse), and gephyrin on $PSD95^+$ spines (inhibitory spine synapse). We have previously shown that the average densities of all these synaptic structures do not differ between ~5-6-month-old pre-plaque hAPP and control (wild type (WT)) mice (Niraula et al., 2023). To assess the dynamics of excitatory synapses and inhibitory synapses, we tracked the

gain and loss of $PSD95^+$ spines (2453 (WT), 2156 (hAPP)) and gephyrin on the shaft and spines (1111 (WT), 1073 (hAPP)).

Under baseline conditions, the gain and loss of all synapse types were balanced. ~2-3% of excitatory synapses were gained, and a similar fraction was lost during baseline conditions (Figure 2A) for both WT and hAPP mice, indicating that amyloid pathology in the visual cortex prior to plaque does not lead to increased loss of excitatory synapses. We found that visual deprivation reduced the gain of excitatory synapses in WT mice. A similar reduction in the gain of these synapses was also seen in hAPP mice (Figure 2A). Overall, we observed a significant effect for light deprivation ($p<0.01$; $F(1, 13) = 15.06$; two-way mixed model ANOVA), but the effect of genotype or the interaction of light and genotype was not significantly different. In contrast to the gain of excitatory synapses, the loss between two sessions did not differ significantly between genotypes or light conditions (remained between 2-3% across conditions; Figure 2A). These results show that excitatory neurons adapt similarly to changes in visually-evoked excitability under amyloid and nonpathological conditions.

Inhibitory synapses are more dynamic than excitatory synapses (Villa et al., 2016). Consistently, we found that ~11% of inhibitory shaft synapses were gained or lost under baseline conditions in WT mice (Figure 2B). The gain and loss were slightly lower in hAPP mice under baseline conditions (~9% gain and ~7% loss; Figure 2B). When visually-evoked activity is reduced by visual deprivation, the gain of new inhibitory shaft synapses was reduced by 2-3% in both WT and hAPP mice. However, the effect of genotype, light, or their interaction is not statistically significantly different, indicating that pre-plaque amyloid pathology under baseline conditions does not affect the gain of new inhibitory shaft synapse.

Visual deprivation elicits disinhibition as a homeostatic adaptation under nonpathological conditions. At the structural level, the loss of inhibitory synapses is increased. Consistently, we found that dark adaptation increased the loss of inhibitory shaft synapses by 63% in WT mice (18% loss; Figure 2B). Interestingly, the loss of inhibitory shaft synapses remained identical (~7% loss) to baseline conditions in hAPP mice (Figure 2B). Consequently, for inhibitory shaft synapses, we found a significant effect for genotype ($p<0.05$, $F(1, 13) = 8.918$), visual deprivation ($p<0.05$, $F(1, 13) = 4.733$), and their interaction ($p<0.05$, $F(1, 13) = 5.215$; two-way mixed model ANOVA; Figure 2B). Inhibitory synapses on spines are more dynamic than inhibitory shaft synapses. Consistent with previous studies, we found that 30-40% of inhibitory synapses on spines were gained or lost under baseline conditions in both WT and hAPP mice; Figure 2C. Though visual deprivation increased the loss of inhibitory spine synapses (net loss: ~50 synapses) in WT mice, we did not find a significant effect of genotype, visual deprivation, or their interaction (Figure 2C). These results show that amyloid pathology selectively disrupts the homeostatic adaptation of inhibitory shaft synapses to changes in excitability.

Since the average gain and loss of inhibitory shaft synapses were balanced, we tested whether this balance persisted at the level of individual dendrites. We found that the correlation between the gain and loss of inhibitory synapses on dendritic branches was significant in WT mice under baseline conditions (Figure 2D). The correlation reduced during visual deprivation and was no longer significant (Figure 2D). However, the difference in correlation between baseline and visual deprivation conditions was not significantly different ($p>0.05$, Fisher r to z transformation). These results indicate that the gain and loss of inhibitory shaft synapses are balanced, and visual deprivation mildly disrupts this balance. The correlation between gain and loss remained close to significance in hAPP mice under both baseline and visual deprivation

conditions, suggesting that amyloid does not disrupt the balance of gain and loss of inhibitory shaft synapses (Figure 2E).

Different inhibitory neuron subtypes project to various dendritic locations. Parvalbumin-expressing interneurons innervate perisomatic and proximal (<40µm from the soma) dendrites, whereas somatostatin-expressing neurons primarily project to distal dendrites (>40 µm from the soma) (Di Cristo et al., 2004). Therefore, we examined whether visual deprivation associated increases in the loss of inhibitory shaft synapses occur differentially depending on dendritic location. The density of inhibitory shaft synapses is the highest closest to the soma and progressively decreases both in WT and hAPP mice (Figure 3A, B). Visual deprivation uniformly and subtly reduces the density of inhibitory shaft synapses at different distances from the soma in WT mice (Figure 3A). In hAPP mice, the density remained identical across all three sessions for all distances from the soma (Figure 3A). Similarly, the increased loss of inhibitory shaft synapses in visual deprivation is evident at all distances from the soma in WT mice (Figure 3A), whereas the loss of synapses was very similar in hAPP mice at all measured distances from the soma (Figure 3A). These results indicate that there may be no dendritic hotspot for disinhibition.

A fraction of inhibitory synapses tends to appear and disappear at the same dendritic locations (Villa et al., 2016). To test whether the structural loss of inhibitory shaft synapse during visual deprivation was driven mainly by the loss of newly acquired inhibitory synapses or those present in both imaging sessions, we compared their relative contribution to the total inhibitory shaft synapse loss (Figure 3B). Of the ~18% synapses that were lost in WT mice in the dark, only 3.6% of them were newly formed synapses in the second session, and the rest (14.8%) were synapses present in the first and second sessions (Figure 3C). In hAPP mice, of the 7% of shaft

synapses that were lost during visual deprivation, ~5% were present in both sessions, and 2% were newly gained synapses (Figure 3C). The loss of newly gained synapses did not differ significantly; therefore, the synapses present in the first two sessions were more stable in hAPP mice (Figure 3C). These results suggest that stable inhibitory shaft synapses become more stabilized in amyloid pathology.

Since the size of gephyrin puncta correlates with the synaptic strength (Villa et al., 2016), we tested whether visual deprivation decreases the average fluorescence intensity of shaft synapses that remained stable across the three sessions. We found no difference in average gephyrin fluorescence between sessions in WT and hAPP mice (Figure 3D). Similar results were obtained when the gephyrin fluorescence was normalized to the cell fill fluorescence (not shown).

Impaired disinhibition in amyloid pathology is not due to altered neuronal activity levels

Since structural dendritic disinhibition is an adaptation triggered by decreased experience-evoked neural activity, a lack of dendritic disinhibition in hAPP mice could be due to increased baseline neuronal activity in these mice compared to WT in the absence of visual experience. Using calcium imaging, we previously found that average spontaneous population activity (mean population dF/F0 of GCaMP6 transients) in the visual cortex recorded without visual experience is not significantly different in~5-6-month-old hAPP mice (Niraula et al., 2023). However, the same average population activity may arise despite differences in the distribution of activity patterns and correlational structure. We analyzed this data set of spontaneous activity over ~228 seconds from 1020 WT and 885 hAPP neurons (Figure 4A). We first classified neurons into different bins of mean dF/F0 to test if the WT and hAPP mice differ in the proportion of neurons

with varied activity profiles without visual experience. We found that the activity distribution is identical between the genotypes (Figure 4A).

An increase in correlated activity in hAPP mice could increase excitability during spontaneous activity and may prevent disinhibition. We obtained the mean correlation for each animal by averaging all the individual neuron-neuron correlations. We found that WT and hAPP mice had a similar average correlation (Figure 4B). Finally, whenever a neuron is activated, its activity level can be determined by the number of functionally connected coactive neurons (node degree). Therefore, neurons with the same average activity could have differential activity levels during each spiking event. We calculated the node degree of a neuron as the number of significant coactive neurons. Two neurons are considered significantly coactive if the number of imaging frames these neurons are coactive is greater than 95% of the cumulative distribution of coactivity generated by 1000 random circular shifts of activities between two neurons. Again, we found no difference in the average node degree of WT and hAPP mice (Figure 4C). These results indicate that impaired disinhibition in hAPP mice may not be due to increased baseline neuronal activity, raising the possibility that amyloid pathology disrupts communication of changes in excitability to inhibitory synapses.

Disrupted clustering of excitatory and inhibitory synapse loss in amyloidosis

Though visual deprivation allowed us to identify the deficit in structural disinhibition, whether amyloid pathology disrupts or alters compensatory inhibitory changes under non-perturbed conditions remains to be tested. The structural plasticity of excitatory and inhibitory synapses are spatially clustered (Chen et al., 2012). However, the extent of excitatory and inhibitory synapse loss clustering is unknown. If communication is impaired, we reasoned that the clustering between excitatory and inhibitory synapse loss would be altered in hAPP mice. To assess this,

we calculated the nearest distance of a lost inhibitory synapse for every lost excitatory synapse (Figure 5A). We found the median nearest distance of lost inhibitory from a lost excitatory synapse in WT mice to be 4 µm. Interestingly, the distribution of nearest distances for hAPP mice was significantly right-shifted compared to WT mice, with a median nearest distance of 7.7 µm (Figure 5B). The mean nearest distance for WT and hAPP mice are 6.8 µm and 13.2 µm, respectively, indicating that there is no nearby inhibitory synapse loss for some excitatory synapse loss in hAPP mice. Since the spread of signaling molecules is limited (typically 3–10 µm), dynamics at greater distances could reflect independent events. These results show that a local loss of inhibitory synapse compensates for the loss of excitatory synapse, and this coupling is disrupted in amyloidosis. We next tested whether similar clustering occurs for the gain of excitatory and inhibitory synapses (Figure 5A). The distribution of the nearest distances of gain of excitatory and inhibitory synapses did not significantly differ between the genotypes, with both WT (median: 5 µm) and hAPP (median: 4 µm) showing close clustering (Figure 5B). We next looked at whether local clustering of inhibitory synapse loss and excitatory synapse loss occurs from the perspective of inhibitory synapses. We calculated the nearest distance of an excitatory synapse loss for every inhibitory synapse loss and found that both WT and hAPP mice did not show close clustering (median WT: 9.4 µm and hAPP: 11 µm) and were not significantly different (Figure 5C).

Reduced clustering of excitatory and inhibitory synapse loss could be due to greater distances between excitatory and inhibitory synapses (despite the same average density) in WT and hAPP mice. Therefore, we measured the nearest distance of an inhibitory synapse to every excitatory synapse and found that they were very similar (median WT: 1.04 µm and hAPP: 0.96 µm) though there is a small but significant left shift for hAPP mice (Figure 5D). Therefore, the

right shift in the distribution of the nearest distances of lost excitatory and inhibitory synapses in hAPP mice is not due to a similar shift in their localization. Together, these results show a selective disruption of the coupling of inhibitory and excitatory synapse loss.

Discussion

Direct visualization of synaptic proteins *in vivo*, repeated imaging of the same synapses, and the use of the visual cortex as a model system, where altering experience-evoked excitability is easy, allowed us to unearth a pathological feature of amyloid that would not be directly evident by visualizing the density or baseline dynamics of synapses either *in vitro* or *in vivo*. Multiple animal studies have uncovered the vulnerability of the visual cortex to AD-related pathology and subtle synaptic dysfunction without overt degeneration could contribute to visual deficits observed in a subset of AD patients (Armstrong, 1996; Grienberger et al., 2012; William et al., 2012; Liebscher et al., 2016; Korzhova et al., 2021; William et al., 2021; Kurucu et al., 2022; Papanikolaou et al., 2022; Niraula et al., 2023).

In amyloid pathology, we identified a selective disruption in the homeostatic structural adaptation of inhibitory synapses on the dendritic shaft. The density or baseline structural dynamics of inhibitory synapses were not significantly perturbed. Furthermore, the baseline structural dynamics of excitatory synapses and their response to altered experience remain unchanged in the same neurons. These results indicate that structural plasticity deficits in the inhibitory system emerge before impairments in the structural plasticity of excitatory synapses in amyloidosis.

Hyper- and hypoactivity of neurons and brain regions in Alzheimer's disease are thought to arise due to defective homeostatic adaptation (Jang and Chung, 2016; Frere and Slutsky, 2018; Styr and Slutsky, 2018). Excitatory synapse loss is thought to be one of the maladaptive

plasticity mechanisms to restrain hyperactivity and could lead to hypoactivity when unchecked. A reduction in excitatory synapse density and brain activity is observed in the later stages of AD (Terry et al., 1991; DeKosky et al., 1996; Dickerson et al., 2005; Celone et al., 2006; Scheff and Price, 2006), indicating an impairment in inhibitory plasticity to compensate for the loss of excitability. Though the order of emergence of hyper- and hypoactivity is still unclear, they must closely follow each other to maintain average activity levels as the total energy budget of the brain is fixed. Consistently, hyper- and hypoactive neurons are present together in mouse models of amyloidosis (Busche et al., 2008; Grienberger et al., 2012; Rudinskiy et al., 2012; Niraula et al., 2023). We recently observed that the increase in neuronal hyper- and hypoactivity occurs at a stage where postsynaptic densities of excitatory and inhibitory synapses are comparable to nonpathological controls (Niraula et al., 2023). Therefore, mechanisms other than excitatory synapse loss, such as changes to the size, stability, and physiology of inhibitory synapses, may contribute to hypoactivity. Consistently, gephyrin levels were found to be higher in amyloid pathology (Hales et al., 2013; Kiss et al., 2016), though the literature is inconsistent on the direction of change in the GABAergic system concerning favoring or opposing hyperactivity. The stability of inhibitory synapses to activity perturbation and local decoupling of excitatory and inhibitory synapse loss indicates that inhibitory synapses in amyloid pathology may not compensate for the reduction in activity levels. On the other hand, local clustering of excitatory and inhibitory synapse gain remains intact in these neurons, thereby balancing an increase in local dendritic excitability. Together, the disrupted dynamic changes of inhibitory synapses favor hypoactivity in the absence of excitatory synapse loss. Since dendritic disinhibition promotes learning-associated plasticity (Letzkus et al., 2015; Mohler and Rudolph, 2017; Artinian and

Lacaille, 2018; Wu et al., 2022), disrupted homeostatic adaptation may also interfere with learning in amyloidosis.

Impaired disinhibition following visual deprivation may arise due to multiple mechanisms. There may be no intrinsic defect in inhibitory synapses that prevent them from undergoing disinhibition. For instance, an elevated baseline activity may not necessitate disinhibition in hAPP mice. However, our spontaneous activity analyses indicate that baseline spontaneous activity (without visual experience) in the visual cortex of hAPP mice at this age is identical to nonpathological controls based on multiple metrics. Therefore, the absence of disinhibition is unlikely due to higher spontaneous activity in hAPP mice in the dark. Alternatively, the neurons in hAPP mice may lack sensors to detect changes in activity. We found that excitatory synapses respond to visual deprivation by reducing gain in the same neurons that exhibit disinhibition deficits. This argues against a general defect in sensing reduction in activity levels. We propose that at least a fraction of inhibitory synapses in neurons of hAPP mice become disengaged from changes in excitatory activity. As a result, these synapses are more stabilized, and local alteration in an excitatory activity does not destabilize them.

Is inhibitory synapse loss a response to or a cause of excitatory synapse loss? The clustered loss of excitation and inhibition is disrupted in hAPP mice only when the distance of the nearest inhibitory synapse loss for every excitatory synapse loss was measured. The distance of the nearest excitatory synapse loss to every inhibitory synapse loss is not locally clustered and did not differ between hAPP and WT mice. These results suggest that loss of excitation may be the driving force for loss of inhibition and not vice versa and is consistent with what has been observed and proposed in other model systems (He et al., 2018). The mechanisms that drive

inhibitory synapse loss following excitatory synapse loss are unclear. Multiple signaling pathways have been shown to enhance or weaken inhibitory synapses following enhancement in excitation (Rutherford et al., 1997; Swanwick et al., 2006; Chen et al., 2012; Flores et al., 2015; Hu et al., 2019; Ravasenga et al., 2022). It is unclear whether these signaling mechanisms are also involved in weakening inhibitory synapses following the weakening of excitatory synapses, possibly by maintaining their co-stability. The direction of clustering of excitatory synapse and inhibitory synapse gain or loss may differ depending on the context. In the learning context, disinhibition is favorable, and consistently, an increase in excitatory synaptic strength was shown to weaken inhibitory synaptic strength (Ravasenga et al., 2022). In the context of homeostasis, the weakening and strengthening of excitatory and inhibitory synapses should occur in the same direction. The reduction in local clustering of excitatory and inhibitory synapse loss may be a consequence of the increased stability of gephyrin from degradation. Multiple posttranslational modifications, particularly phosphorylation, influence gephyrin stability (Tyagarajan et al., 2011; Kuhse et al., 2012; Kalbouneh et al., 2014; Zacchi et al., 2014; Flores et al., 2015; Wang et al., 2015; Zhou et al., 2021). Kinases that phosphorylate gephyrin and alter its stability, such as CDK5, is dysregulated in AD (Kiss et al., 2020). Whether CDK5-mediated phosphorylation or other posttranslational mechanisms are involved in disrupted disinhibition remains to be tested.

Visual deprivation has been shown to elicit rapid disinhibition due to reduced activity of parvalbumin-expressing interneurons (Hengen et al., 2013; Kuhlman et al., 2013; Barnes et al., 2015). Parvalbumin-expressing neurons primarily target perisomatic regions and proximal dendrites, whereas somatostatin-expressing interneurons target distal dendrites (Di Cristo et al., 2004). However, their localization is not mutually exclusive. We did not find a spatially restricted dendritic disinhibition, and the reduction of synapse density by deprivation appeared to

be more uniform across the length of the dendrite. Future work with cell-type specific labeling is required to test whether structural disinhibition happens at both parvalbumin and somatostatin innervations.

Author contributions: SN performed the experiments. SN and JS performed data analyses. SSY and JS initiated the concept and designed the experiments. JS wrote the paper and supervised the research.

Conflict of interest: The authors declare no competing financial interests.

Acknowledgment: This work was supported by a grant from the National Institutes of Health (Grant No. RO1AG064067) to JS and RF1AG054320, R01AG053041 to SSY. We thank the members of the Subramanian lab for their comments on the manuscript.

References

Armstrong RA (1996) Visual field defects in Alzheimer's disease patients may reflect differential pathology in the primary visual cortex. Optom Vis Sci 73:677-682.

Artinian J, Lacaille JC (2018) Disinhibition in learning and memory circuits: New vistas for somatostatin interneurons and long-term synaptic plasticity. Brain Res Bull 141:20-26.

Barnes SJ, Sammons RP, Jacobsen RI, Mackie J, Keller GB, Keck T (2015) Subnetwork-Specific Homeostatic Plasticity in Mouse Visual Cortex In Vivo. Neuron 86:1290-1303.

Barnes SJ, Franzoni E, Jacobsen RI, Erdelyi F, Szabo G, Clopath C, Keller GB, Keck T (2017) Deprivation-Induced Homeostatic Spine Scaling In Vivo Is Localized to Dendritic Branches that Have Undergone Recent Spine Loss. Neuron 96:871-882 e875.

Busche MA, Konnerth A (2016) Impairments of neural circuit function in Alzheimer's disease. Philos Trans R Soc Lond B Biol Sci 371.

Busche MA, Eichhoff G, Adelsberger H, Abramowski D, Wiederhold KH, Haass C, Staufenbiel M, Konnerth A, Garaschuk O (2008) Clusters of hyperactive neurons near amyloid plaques in a mouse model of Alzheimer's disease. Science 321:1686-1689.

Celone KA, Calhoun VD, Dickerson BC, Atri A, Chua EF, Miller SL, DePeau K, Rentz DM, Selkoe DJ, Blacker D, Albert MS, Sperling RA (2006) Alterations in memory networks in mild cognitive impairment and Alzheimer's disease: an independent component analysis. J Neurosci 26:10222-10231.

Chen JL, Villa KL, Cha JW, So PT, Kubota Y, Nedivi E (2012) Clustered dynamics of inhibitory synapses and dendritic spines in the adult neocortex. Neuron 74:361-373.

Chen TW, Wardill TJ, Sun Y, Pulver SR, Renninger SL, Baohan A, Schreiter ER, Kerr RA, Orger MB, Jayaraman V, Looger LL, Svoboda K, Kim DS (2013) Ultrasensitive fluorescent proteins for imaging neuronal activity. Nature 499:295-300.

Coleman JE, Nahmani M, Gavornik JP, Haslinger R, Heynen AJ, Erisir A, Bear MF (2010) Rapid structural remodeling of thalamocortical synapses parallels experience-dependent functional plasticity in mouse primary visual cortex. J Neurosci 30:9670-9682.

DeKosky ST, Scheff SW, Styren SD (1996) Structural correlates of cognition in dementia: quantification and assessment of synapse change. Neurodegeneration 5:417-421.

Di Cristo G, Wu C, Chattopadhyaya B, Ango F, Knott G, Welker E, Svoboda K, Huang ZJ (2004) Subcellular domain-restricted GABAergic innervation in primary visual cortex in the absence of sensory and thalamic inputs. Nat Neurosci 7:1184-1186.

Dickerson BC, Salat DH, Greve DN, Chua EF, Rand-Giovannetti E, Rentz DM, Bertram L, Mullin K, Tanzi RE, Blacker D, Albert MS, Sperling RA (2005) Increased hippocampal activation in mild cognitive impairment compared to normal aging and AD. Neurology 65:404-411.

Dorostkar MM, Zou C, Blazquez-Llorca L, Herms J (2015) Analyzing dendritic spine pathology in Alzheimer's disease: problems and opportunities. Acta Neuropathol 130:1-19.

Flores CE, Nikonenko I, Mendez P, Fritschy JM, Tyagarajan SK, Muller D (2015) Activity-dependent inhibitory synapse remodeling through gephyrin phosphorylation. Proc Natl Acad Sci U S A 112:E65-72.

Frere S, Slutsky I (2018) Alzheimer's Disease: From Firing Instability to Homeostasis Network Collapse. Neuron 97:32-58.

Gainey MA, Feldman DE (2017) Multiple shared mechanisms for homeostatic plasticity in rodent somatosensory and visual cortex. Philos Trans R Soc Lond B Biol Sci 372.

Garcia-Marin V, Blazquez-Llorca L, Rodriguez JR, Boluda S, Muntane G, Ferrer I, Defelipe J (2009) Diminished perisomatic GABAergic terminals on cortical neurons adjacent to amyloid plaques. Front Neuroanat 3:28.

Goel A, Lee HK (2007) Persistence of experience-induced homeostatic synaptic plasticity through adulthood in superficial layers of mouse visual cortex. J Neurosci 27:6692-6700.

Grienberger C, Rochefort NL, Adelsberger H, Henning HA, Hill DN, Reichwald J, Staufenbiel M, Konnerth A (2012) Staged decline of neuronal function in vivo in an animal model of Alzheimer's disease. Nat Commun 3:774.

Hales CM, Rees H, Seyfried NT, Dammer EB, Duong DM, Gearing M, Montine TJ, Troncoso JC, Thambisetty M, Levey AI, Lah JJ, Wingo TS (2013) Abnormal gephyrin immunoreactivity associated with Alzheimer disease pathologic changes. J Neuropathol Exp Neurol 72:1009-1015.

Harris JA, Devidze N, Halabisky B, Lo I, Thwin MT, Yu GQ, Bredesen DE, Masliah E, Mucke L (2010) Many neuronal and behavioral impairments in transgenic mouse models of Alzheimer's disease are independent of caspase cleavage of the amyloid precursor protein. J Neurosci 30:372-381.

He HY, Shen W, Zheng L, Guo X, Cline HT (2018) Excitatory synaptic dysfunction cell-autonomously decreases inhibitory inputs and disrupts structural and functional plasticity. Nat Commun 9:2893.

Hengen KB, Lambo ME, Van Hooser SD, Katz DB, Turrigiano GG (2013) Firing rate homeostasis in visual cortex of freely behaving rodents. Neuron 80:335-342.

Hofer SB, Mrsic-Flogel TD, Bonhoeffer T, Hubener M (2009) Experience leaves a lasting structural trace in cortical circuits. Nature 457:313-317.

Hollnagel JO, Elzoheiry S, Gorgas K, Kins S, Beretta CA, Kirsch J, Kuhse J, Kann O, Kiss E (2019) Early alterations in hippocampal perisomatic GABAergic synapses and network oscillations in a mouse model of Alzheimer's disease amyloidosis. PLoS One 14:e0209228.

Hu HY, Kruijssen DLH, Frias CP, Rozsa B, Hoogenraad CC, Wierenga CJ (2019) Endocannabinoid Signaling Mediates Local Dendritic Coordination between Excitatory and Inhibitory Synapses. Cell Rep 27:666-675 e665.

Jang SS, Chung HJ (2016) Emerging Link between Alzheimer's Disease and Homeostatic Synaptic Plasticity. Neural Plast 2016:7969272.

Jimenez-Balado J, Eich TS (2021) GABAergic dysfunction, neural network hyperactivity and memory impairments in human aging and Alzheimer's disease. Semin Cell Dev Biol 116:146-159.

Kalbouneh H, Schlicksupp A, Kirsch J, Kuhse J (2014) Cyclin-dependent kinase 5 is involved in the phosphorylation of gephyrin and clustering of GABAA receptors at inhibitory synapses of hippocampal neurons. PLoS One 9:e104256.

Keck T, Mrsic-Flogel TD, Vaz Afonso M, Eysel UT, Bonhoeffer T, Hubener M (2008) Massive restructuring of neuronal circuits during functional reorganization of adult visual cortex. Nat Neurosci 11:1162-1167.

Keck T, Keller GB, Jacobsen RI, Eysel UT, Bonhoeffer T, Hubener M (2013) Synaptic scaling and homeostatic plasticity in the mouse visual cortex in vivo. Neuron 80:327-334.

Keck T, Scheuss V, Jacobsen RI, Wierenga CJ, Eysel UT, Bonhoeffer T, Hubener M (2011) Loss of sensory input causes rapid structural changes of inhibitory neurons in adult mouse visual cortex. Neuron 71:869-882.

Kiss E, Gorgas K, Schlicksupp A, Gross D, Kins S, Kirsch J, Kuhse J (2016) Biphasic Alteration of the Inhibitory Synapse Scaffold Protein Gephyrin in Early and Late Stages of an Alzheimer Disease Model. Am J Pathol 186:2279-2291.

Kiss E, Groeneweg F, Gorgas K, Schlicksupp A, Kins S, Kirsch J, Kuhse J (2020) Amyloid-beta Fosters p35/CDK5 Signaling Contributing to Changes of Inhibitory Synapses in Early Stages of Cerebral Amyloidosis. J Alzheimers Dis 74:1167-1187.

Korzhova V, Marinkovic P, Njavro JR, Goltstein PM, Sun F, Tahirovic S, Herms J, Liebscher S (2021) Long-term dynamics of aberrant neuronal activity in awake Alzheimer's disease transgenic mice. Commun Biol 4:1368.

Kuhlman SJ, Olivas ND, Tring E, Ikrar T, Xu X, Trachtenberg JT (2013) A disinhibitory microcircuit initiates critical-period plasticity in the visual cortex. Nature 501:543-546.

Kuhse J, Kalbouneh H, Schlicksupp A, Mukusch S, Nawrotzki R, Kirsch J (2012) Phosphorylation of gephyrin in hippocampal neurons by cyclin-dependent kinase CDK5 at Ser-270 is dependent on collybistin. J Biol Chem 287:30952-30966.

Kurucu H, Colom-Cadena M, Davies C, Wilkins L, King D, Rose J, Tzioras M, Tulloch JH, Smith C, Spires-Jones TL (2022) Inhibitory synapse loss and accumulation of amyloid beta in inhibitory presynaptic terminals in Alzheimer's disease. Eur J Neurol 29:1311-1323.

Lee HK, Kirkwood A (2019) Mechanisms of Homeostatic Synaptic Plasticity in vivo. Front Cell Neurosci 13:520.

Letzkus JJ, Wolff SB, Luthi A (2015) Disinhibition, a Circuit Mechanism for Associative Learning and Memory. Neuron 88:264-276.

Liebscher S, Meyer-Luehmann M (2012) A Peephole into the Brain: Neuropathological Features of Alzheimer's Disease Revealed by in vivo Two-Photon Imaging. Front Psychiatry 3:26.

Liebscher S, Keller GB, Goltstein PM, Bonhoeffer T, Hubener M (2016) Selective Persistence of Sensorimotor Mismatch Signals in Visual Cortex of Behaving Alzheimer's Disease Mice. Curr Biol 26:956-964.

Melgosa-Ecenarro L, Doostdar N, Radulescu CI, Jackson JS, Barnes SJ (2023) Pinpointing the locus of GABAergic vulnerability in Alzheimer's disease. Semin Cell Dev Biol 139:35-54.

Mitew S, Kirkcaldie MT, Dickson TC, Vickers JC (2013) Altered synapses and gliotransmission in Alzheimer's disease and AD model mice. Neurobiol Aging 34:2341-2351.

Mohler H, Rudolph U (2017) Disinhibition, an emerging pharmacology of learning and memory. F1000Res 6.

Montero-Crespo M, Dominguez-Alvaro M, Alonso-Nanclares L, DeFelipe J, Blazquez-Llorca L (2021) Three-dimensional analysis of synaptic organization in the hippocampal CA1 field in Alzheimer's disease. Brain 144:553-573.

Niraula S, Doderer JJ, Indulkar S, Berry KP, Hauser WL, L'Esperance OJ, Deng JZ, Keeter G, Rouse AG, Subramanian J (2023) Excitation-inhibition imbalance disrupts visual familiarity in amyloid and non-pathology conditions. Cell Rep 42:111946.

Pachitariu M, Stringer C, Dipoppa M, Schröder S, Rossi LF, Dalgleish H, Carandini M, Harris KD (2017) Suite2p: beyond 10,000 neurons with standard two-photon microscopy. bioRxiv.

Palop JJ, Mucke L (2016) Network abnormalities and interneuron dysfunction in Alzheimer disease. Nat Rev Neurosci 17:777-792.

Palop JJ, Mucke L, Roberson ED (2011) Quantifying biomarkers of cognitive dysfunction and neuronal network hyperexcitability in mouse models of Alzheimer's disease: depletion of calcium-dependent proteins and inhibitory hippocampal remodeling. Methods Mol Biol 670:245-262.

Papanikolaou A, Rodrigues FR, Holeniewska J, Phillips KG, Saleem AB, Solomon SG (2022) Plasticity in visual cortex is disrupted in a mouse model of tauopathy. Commun Biol 5:77.

Petrache AL, Rajulawalla A, Shi A, Wetzel A, Saito T, Saido TC, Harvey K, Ali AB (2019) Aberrant Excitatory-Inhibitory Synaptic Mechanisms in Entorhinal Cortex Microcircuits During the Pathogenesis of Alzheimer's Disease. Cereb Cortex 29:1834-1850.

Ravasenga T, Ruben M, Regio V, Polenghi A, Petrini EM, Barberis A (2022) Spatial regulation of coordinated excitatory and inhibitory synaptic plasticity at dendritic synapses. Cell Rep 38:110347.

Rudinskiy N, Hawkes JM, Betensky RA, Eguchi M, Yamaguchi S, Spires-Jones TL, Hyman BT (2012) Orchestrated experience-driven Arc responses are disrupted in a mouse model of Alzheimer's disease. Nat Neurosci 15:1422-1429.

Ruiter M, Herstel LJ, Wierenga CJ (2020) Reduction of Dendritic Inhibition in CA1 Pyramidal Neurons in Amyloidosis Models of Early Alzheimer's Disease. J Alzheimers Dis 78:951-964.

Ruiter M, Lutzkendorf C, Liang J, Wierenga CJ (2021) Amyloid-beta Oligomers Induce Only Mild Changes to Inhibitory Bouton Dynamics. J Alzheimers Dis Rep 5:153-160.

Rutherford LC, DeWan A, Lauer HM, Turrigiano GG (1997) Brain-derived neurotrophic factor mediates the activity-dependent regulation of inhibition in neocortical cultures. J Neurosci 17:4527-4535.

Sammons RP, Clopath C, Barnes SJ (2018) Size-Dependent Axonal Bouton Dynamics following Visual Deprivation In Vivo. Cell Rep 22:576-584.

Scaduto P, Lauterborn JC, Cox CD, Fracassi A, Zeppillo T, Gutierrez BA, Keene CD, Crane PK, Mukherjee S, Russell WK, Taglialatela G, Limon A (2023) Functional excitatory to inhibitory synaptic imbalance and loss of cognitive performance in people with Alzheimer's disease neuropathologic change. Acta Neuropathol 145:303-324.

Scheff SW, Price DA (2006) Alzheimer's disease-related alterations in synaptic density: neocortex and hippocampus. J Alzheimers Dis 9:101-115.

Schmid LC, Mittag M, Poll S, Steffen J, Wagner J, Geis HR, Schwarz I, Schmidt B, Schwarz MK, Remy S, Fuhrmann M (2016) Dysfunction of Somatostatin-Positive Interneurons Associated with Memory Deficits in an Alzheimer's Disease Model. Neuron 92:114-125.

Shimojo M, Takuwa H, Takado Y, Tokunaga M, Tsukamoto S, Minatohara K, Ono M, Seki C, Maeda J, Urushihata T, Minamihisamatsu T, Aoki I, Kawamura K, Zhang MR, Suhara T, Sahara N, Higuchi M (2020) Selective Disruption of Inhibitory Synapses Leading to Neuronal Hyperexcitability at an Early Stage of Tau Pathogenesis in a Mouse Model. J Neurosci 40:3491-3501.

Sos KE, Mayer MI, Takacs VT, Major A, Bardoczi Z, Beres BM, Szeles T, Saito T, Saido TC, Mody I, Freund TF, Nyiri G (2020) Amyloid beta induces interneuron-specific changes in the hippocampus of APPNL-F mice. PLoS One 15:e0233700.

Styr B, Slutsky I (2018) Imbalance between firing homeostasis and synaptic plasticity drives early-phase Alzheimer's disease. Nat Neurosci 21:463-473.

Subramanian J, Dye L, Morozov A (2013) Rap1 signaling prevents L-type calcium channel-dependent neurotransmitter release. J Neurosci 33:7245-7252.

Subramanian J, Savage JC, Tremblay ME (2020) Synaptic Loss in Alzheimer's Disease: Mechanistic Insights Provided by Two-Photon in vivo Imaging of Transgenic Mouse Models. Front Cell Neurosci 14:592607.

Subramanian J, Michel K, Benoit M, Nedivi E (2019) CPG15/Neuritin Mimics Experience in Selecting Excitatory Synapses for Stabilization by Facilitating PSD95 Recruitment. Cell Rep 28:1584-1595 e1585.

Sun YJ, Espinosa JS, Hoseini MS, Stryker MP (2019) Experience-dependent structural plasticity at pre- and postsynaptic sites of layer 2/3 cells in developing visual cortex. Proc Natl Acad Sci U S A 116:21812-21820.

Swanwick CC, Murthy NR, Kapur J (2006) Activity-dependent scaling of GABAergic synapse strength is regulated by brain-derived neurotrophic factor. Mol Cell Neurosci 31:481-492.

Terry RD, Masliah E, Salmon DP, Butters N, DeTeresa R, Hill R, Hansen LA, Katzman R (1991) Physical basis of cognitive alterations in Alzheimer's disease: synapse loss is the major correlate of cognitive impairment. Ann Neurol 30:572-580.

Turrigiano G (2012) Homeostatic synaptic plasticity: local and global mechanisms for stabilizing neuronal function. Cold Spring Harb Perspect Biol 4:a005736.

Tyagarajan SK, Ghosh H, Yevenes GE, Nikonenko I, Ebeling C, Schwerdel C, Sidler C, Zeilhofer HU, Gerrits B, Muller D, Fritschy JM (2011) Regulation of GABAergic synapse formation and plasticity by GSK3beta-dependent phosphorylation of gephyrin. Proc Natl Acad Sci U S A 108:379-384.

Umeda T, Kimura T, Yoshida K, Takao K, Fujita Y, Matsuyama S, Sakai A, Yamashita M, Yamashita Y, Ohnishi K, Suzuki M, Takuma H, Miyakawa T, Takashima A, Morita T, Mori H, Tomiyama T (2017) Mutation-induced loss of APP function causes GABAergic depletion in recessive familial Alzheimer's disease: analysis of Osaka mutation-knockin mice. Acta Neuropathol Commun 5:59.

van Versendaal D, Rajendran R, Saiepour MH, Klooster J, Smit-Rigter L, Sommeijer JP, De Zeeuw CI, Hofer SB, Heimel JA, Levelt CN (2012) Elimination of inhibitory synapses is a major component of adult ocular dominance plasticity. Neuron 74:374-383.

Villa KL, Berry KP, Subramanian J, Cha JW, Oh WC, Kwon HB, Kubota Y, So PT, Nedivi E (2016) Inhibitory Synapses Are Repeatedly Assembled and Removed at Persistent Sites In Vivo. Neuron 89:756-769.

Wang CY, Lin HC, Song YP, Hsu YT, Lin SY, Hsu PC, Lin CH, Hung CC, Hsu MC, Kuo YM, Lee YJ, Hsu CY, Lee YH (2015) Protein kinase C-dependent growth-associated protein 43 phosphorylation regulates gephyrin aggregation at developing GABAergic synapses. Mol Cell Biol 35:1712-1726.

William CM, Stern MA, Pei X, Saqran L, Ramani M, Frosch MP, Hyman BT (2021) Impairment of visual cortical plasticity by amyloid-beta species. Neurobiol Dis 154:105344.

William CM, Andermann ML, Goldey GJ, Roumis DK, Reid RC, Shatz CJ, Albers MW, Frosch MP, Hyman BT (2012) Synaptic plasticity defect following visual deprivation in Alzheimer's disease model transgenic mice. J Neurosci 32:8004-8011.

Wu YK, Miehl C, Gjorgjieva J (2022) Regulation of circuit organization and function through inhibitory synaptic plasticity. Trends Neurosci 45:884-898.

Zacchi P, Antonelli R, Cherubini E (2014) Gephyrin phosphorylation in the functional organization and plasticity of GABAergic synapses. Front Cell Neurosci 8:103.

Zhou L, Kiss E, Demmig R, Kirsch J, Nawrotzki RA, Kuhse J (2021) Binding of gephyrin to microtubules is regulated by its phosphorylation at Ser270. Histochem Cell Biol 156:5-18.

Zhou Y, Lai B, Gan WB (2017) Monocular deprivation induces dendritic spine elimination in the developing mouse visual cortex. Sci Rep 7:4977.

Figure legends

Figure 1. *In vivo* structural imaging of homeostatic synaptic plasticity. A. Timeline of imaging. In utero electroporation (IUE) of plasmids expressing Cre recombinase and Cre-dependent markers was performed on embryonic days 15.5-16.5. A cranial window was placed at ~ five months old, and two weeks later, optical intrinsic signal (OIS) imaging was performed to map the visual cortex. Two-photon imaging of neurons in the mapped visual cortex was performed in three imaging sessions (S1, S2, and S3). Each imaging session was separated by one week, and mice were housed in 24-hour darkness (24 D) between S2 and S3. At all other times, they were housed under 12-hour light: 12-hour dark (12L:12D) cycle. **B.** A 5mm cranial window (left) and a magnitude map (blue oval) of intrinsic signal (right). **C-G.** Pseudocolored images of the same dendritic segments from the three sessions (red: cell fill; green: PSD95; gray: Gephyrin). PSD95 and gephyrin channels are shown below the merged images. Gain and loss (blue arrows (C-F) of excitatory synapses (gain – C and loss – D), inhibitory synapse on shaft (gain – E and loss – F), and inhibitory synapses on spines (blue arrow - gain in S1 loss in S2, yellow arrow – loss, G).

Figure 2. Inhibitory but not excitatory synaptic structural adaptation deficits in amyloid pathology. A-C. Percentage of excitatory synapses (A), inhibitory synapses on shaft (B), and inhibitory synapses on spines (C) gained (left) or lost (right) in baseline (light) and visual deprivation (dark) conditions in wild type (WT) and hAPP mice. Circles represent individual neuron values. n = 7 neurons (5 WT mice), 8 neurons (7 hAPP mice). Two-way mixed model ANOVA was used to test the effect of light vs. dark (L), genotype (G), and their interaction (G X L). ns: not significant. Data are presented as mean ± SEM. **D-E**. Correlation of percentage gain

and loss of inhibitory shaft synapses on individual dendrites in WT (D) and hAPP (E) mice in baseline and visual deprivation conditions n = 54 dendrites (WT) and 48 dendrites (hAPP).

Figure 3. Characterization of dendritic shaft structural disinhibition. A. (Left) Density of inhibitory shaft synapses at different distances from soma from the three imaging sessions (S1, S2, and S3) in wild type (WT) and hAPP mice. (Right) Percentage loss of inhibitory shaft synapses at different distances from the soma in baseline (light) and visual deprivation (dark) conditions in WT and hAPP mice. n = 54 dendrites (WT) and 48 dendrites (hAPP). **B**. Representation of an inhibitory shaft synapse that was present in the first two imaging sessions (stable-light) but was lost in the third session (left) and a synapse that appeared in the second imaging session (gained-light) and disappeared (right). **C**. Percentage of stable and gained inhibitory shaft synapses lost following visual deprivation (dark). n = 7 (WT), and 8 (hAPP) neurons. ** $p<0.01$, one-way MANOVA. **D.** Average fluorescence (arbitrary fluorescence units (AFU)) of inhibitory shaft synapses in the three sessions in WT and hAPP mice. Circles represent neuron values, and data are presented as mean ± SEM.

Figure 4. Baseline spontaneous activity is not different in WT and hAPP mice. A. Standard deviation projection image of a representative imaging field of neurons expressing GCaMP6s (top). Calcium transients (dF/F0) of three color matched circled neurons with varying levels of activity. Percentage of neurons in different dF/F0 bins in WT and hAPP mice (bottom). **B**. Representative correlation matrices of WT and hAPP mice. (Bottom) Mean correlation from all mice. **C**. Representative images of two neurons that are functionally connected (top) or not connected (bottom) and the average node degree (right). n = 10 WT (1020 neurons) and 9 hAPP mice (885 neurons).

Figure 5. Local clustering of excitatory and inhibitory synapse loss is disrupted in hAPP mice. A. A representative illustration of nearest neighbor analysis. "A" is an excitatory synapse that disappeared between sessions 1 (S1) and 2 (S2). "a" and "b" are two inhibitory synapses that disappeared during the same interval. "a" will be the nearest inhibitory synapse loss for the excitatory synapse "A" in this dendritic segment. Similarly, a' is the nearest gained inhibitory synapse to A', a gained excitatory synapse. For every excitatory synapse lost, the distance to the nearest inhibitory synapse loss was calculated. Similarly, for every gained excitatory synapse, the distance to the nearest inhibitory synapse gain was calculated. **B.** (Left) Cumulative probability distribution (CPD) of nearest neighbor distances of lost inhibitory synapses to all lost excitatory synapses. n = 71 (WT) and 48 (hAPP) lost excitatory synapses, $P<0.05$, Kolmogorov-Smirnov (KS) test. (Right) CPD of nearest neighbor distances of gained inhibitory synapses to all gained excitatory synapses. n = 61 (WT) and 54 (hAPP) gained excitatory synapses, ns – not significant, KS test. **C.** (Left). "a" is the nearest excitatory synapse lost to "A", a lost inhibitory synapse. (Right) CPD of nearest neighbor distances of lost excitatory synapses to all lost inhibitory synapses. ns – not significant, KS test. n = 158 (WT) and 71 (hAPP) lost inhibitory synapses. **D.** (Left). "x" is the nearest inhibitory synapse to "A", the excitatory synapse. (Right) CPD of nearest neighbor distances of inhibitory synapses to all excitatory synapses. $p<0.05$ KS test, n = 2453 (WT) and 1851 (hAPP) excitatory synapses.

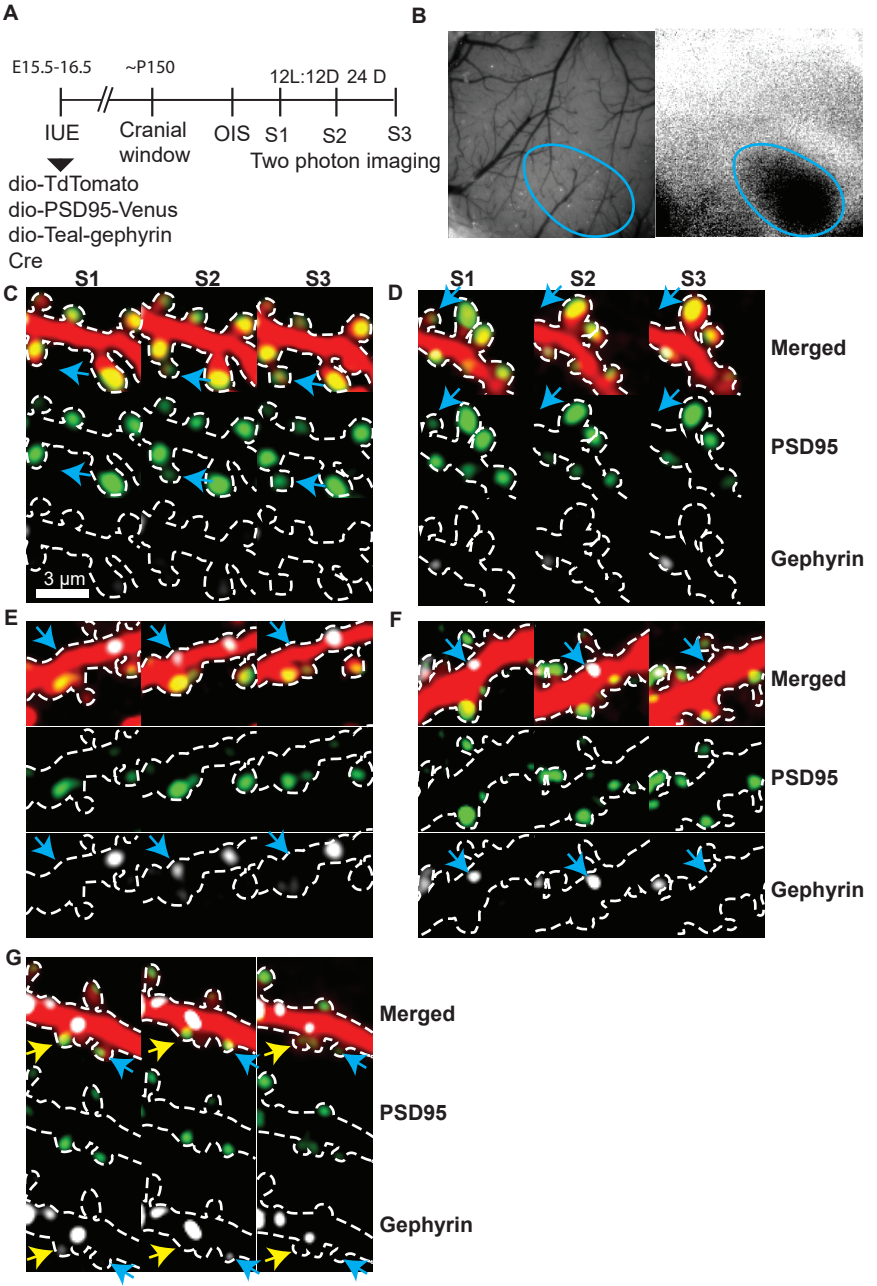
A
E15.5-16.5
~P150
12L:12D 24 D
IUE
Cranial window
OIS
S1
S2
S3
Two photon imaging
dio-TdTomato
dio-PSD95-Venus
dio-Teal-gephyrin
Cre
B
C
S1
S2
S3
3 µm
D
S1
S2
S3
Merged
PSD95
Gephyrin
E
F
Merged
PSD95
Gephyrin
G
Merged
PSD95
Gephyrin

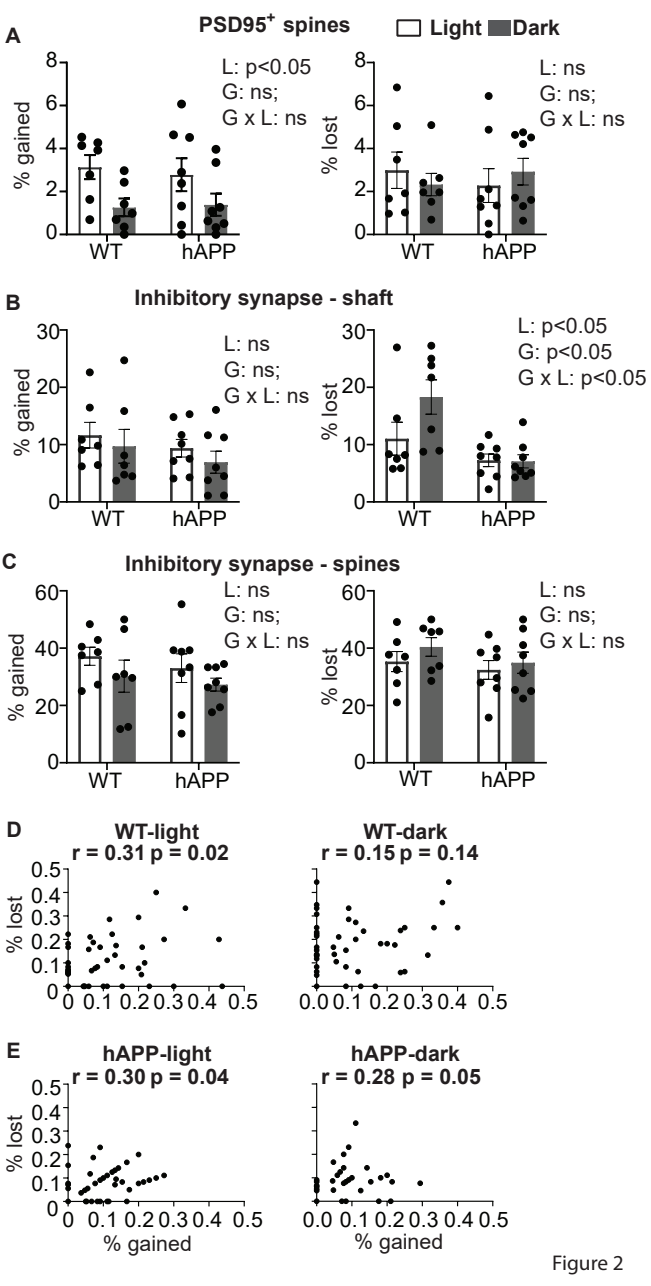
A
PSD95+ spines
Light
Dark
% gained
L: p<0.05
G: ns;
G x L: ns
WT
hAPP
% lost
L: ns
G: ns;
G x L: ns
B
Inhibitory synapse - shaft
% gained
L: ns
G: ns;
G x L: ns
% lost
L: p<0.05
G: p<0.05
G x L: p<0.05
C
Inhibitory synapse - spines
% gained
L: ns
G: ns;
G x L: ns
% lost
L: ns
G: ns;
G x L: ns
D
WT-light
r = 0.31 p = 0.02
WT-dark
r = 0.15 p = 0.14
% lost
E
hAPP-light
r = 0.30 p = 0.04
hAPP-dark
r = 0.28 p = 0.05
% lost
% gained
% gained

Figure 2

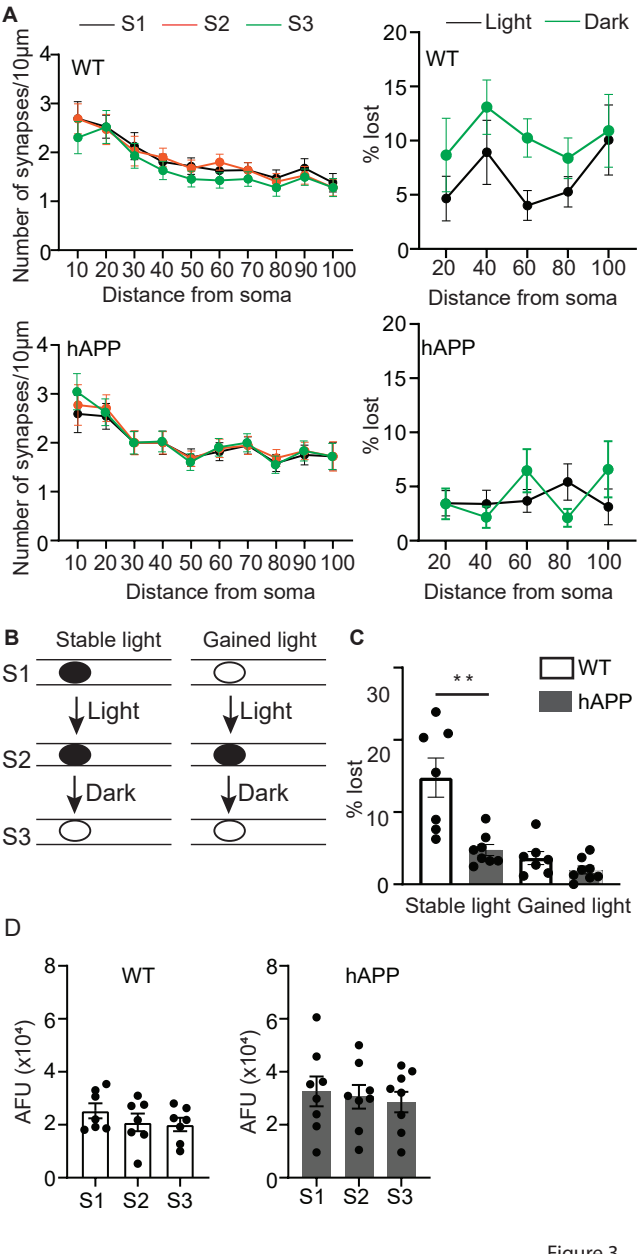
A
S1
S2
S3
WT
Number of synapses/10µm
Distance from soma
Light
Dark
% lost
hAPP
B
Stable light
Gained light
Light
Dark
C
WT
hAPP
**
D
AFU (x10⁴)

Figure 3

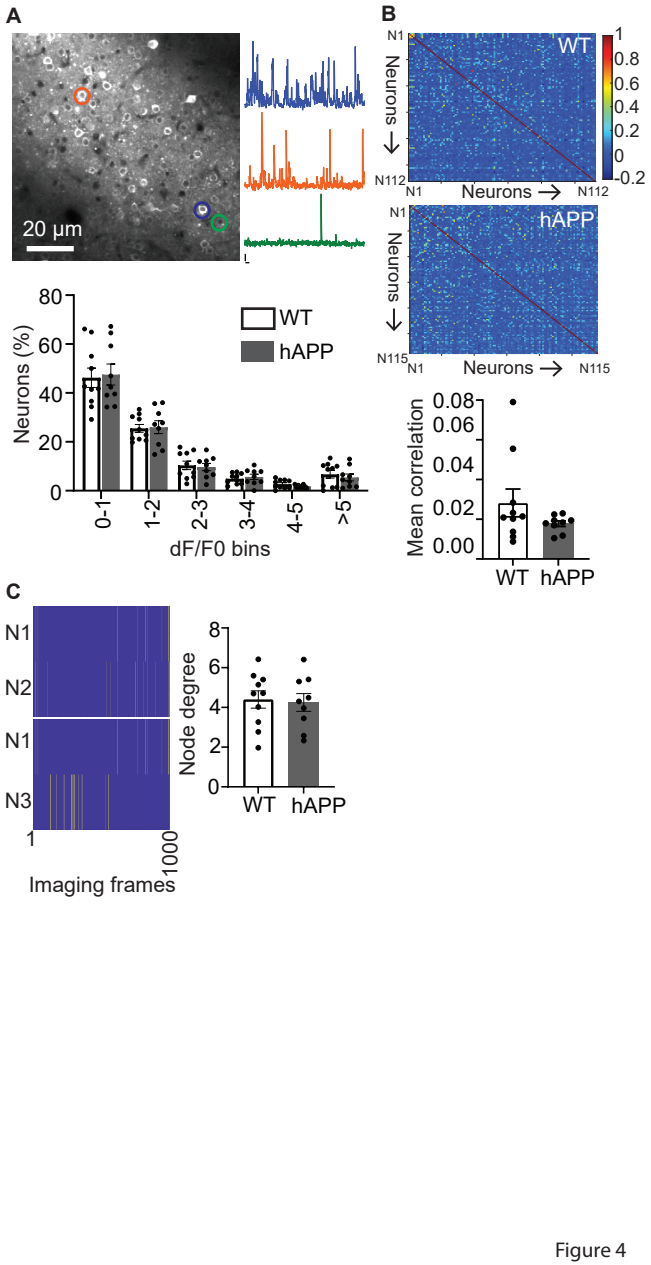
A
20 µm
B
WT
hAPP
Neurons
N1
N112
N115
1
0.8
0.6
0.4
0.2
0
-0.2
Neurons (%)
dF/F0 bins
0-1
1-2
2-3
3-4
4-5
>5
Mean correlation
0.08
0.06
0.04
0.02
0.00
C
N1
N2
N3
1000
Imaging frames
Node degree

Figure 4

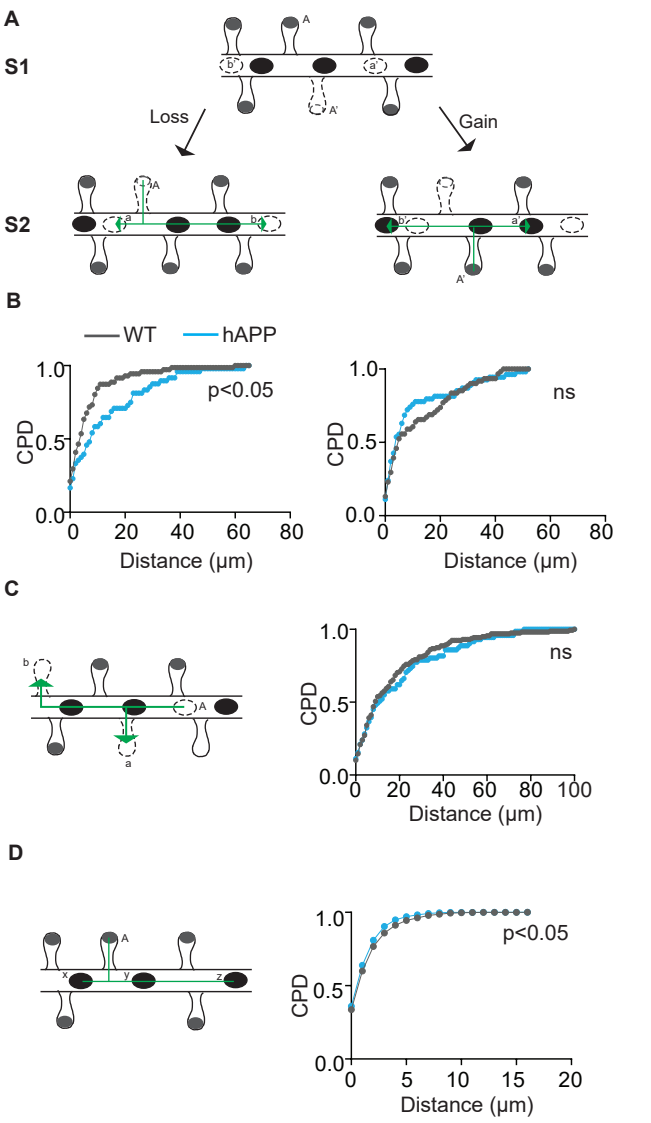
A
S1
b'
A'
a'
Loss
Gain
S2
A
a
b
b
a
A'
B
WT
hAPP
1.0
0.5
0.0
CPD
p<0.05
0
20
40
60
80
Distance (μm)
1.0
0.5
0.0
CPD
ns
0
20
40
60
80
Distance (μm)
C
b
A
a
1.0
0.5
0.0
CPD
ns
0
20
40
60
80
100
Distance (μm)
D
A
x
y
z
1.0
0.5
0.0
CPD
p<0.05
0
5
10
15
20
Distance (μm)

Figure 5